# Modelling and Design Optimisation of a High Bandwidth and High Precision Optical Current Sensor Based on the Faraday Effect

**Conference Paper**

**Author(s):**
Rietmann, Stefan (iD); Schlesinger, Richard (iD); Biela, Jürgen (iD)

# Modelling and Design Optimisation of a High Bandwidth and High Precision Optical Current Sensor Based on the Faraday Effect

Stefan Rietmann, Richard Schlesinger and Jürgen Biela
Laboratory for High Power Electronic Systems (HPE), ETH Zurich
rietmann@hpe.ee.ethz.ch

## Keywords

## Abstract

A magneto-optical current measurement system based on the Faraday effect is evaluated for measuring fast pulse currents in high power applications. The current measurement system is based on the interaction of the magnetic field, generated by the current, and a beam of light propagating through magneto-optical material which is in close proximity to the current conductor. A high local magnetic field per ampère current inside the optical path is required to improve the accuracy and the sensitivity of the optical current measurement sensor.

In this paper, the relation between the conductor geometry and the local magnetic field distribution is analytically modelled resulting in the geometry factor $K_g$. The analytical model enables an optimisation of the busbar geometry to increase the overall probe sensitivity and the accuracy of the optical current measurement system.

## 1 Introduction

For measuring currents in applications with high bandwidth and high accuracy requirements, optical current measurement systems are a promising concept. Depending on the considered application, a very high bandwidth of multiple MHz [1], a high insulation voltage, and a high CMRR are required. In addition, a low insertion impedance due to the probe is desirable especially for pulsed current applications with fast pulse rise times ($t_r \leq 1\,\mu s$) and high current amplitudes ($I_{peak} \geq 1\,kA$). An optical current measurement system with a magneto-optical current sensor (MOCS) based on the Faraday effect satisfies these requirements.

A magneto-optical current sensor is made of magneto-optical (MO) material. The MOCS is placed closely to a current-carrying conductor which generates a magnetic field, as shown in Fig. 1a). Coherent and linearly polarised light propagating through the MOCS experiences a change of its polarisation orientation. This change is proportional to the amplitude of the magnetic field parallel to the light in the MOCS. Ideally, only the plane of polarisation of the propagating light is rotated, but its polarisation state remains unchanged [2]. The Faraday effect can generally be described by the optical rotation $\Theta_F$:

$$\Theta_F = \mathcal{V} \int_{\mathcal{P}} \mu_0 \mu_r \vec{H}_{opt} \cdot \mathrm{d}\vec{l}_{opt} = \mathcal{V} \int_{\mathcal{P}} \vec{B}_{opt} \cdot \mathrm{d}\vec{l}_{opt} = \mathcal{V} I_m \int_{\mathcal{P}} \vec{b}_g \cdot \mathrm{d}\vec{l}_{opt} = \mathcal{V} I_m K_g \tag{1}$$

where $\mathcal{V}$ is the Verdet constant, $\vec{l}_{opt}$ denotes the direction of the optical path $\mathcal{P}$ in the MOCS and $\vec{H}_{opt}$ is the magnetic field in the optical path. The term $\vec{b}_g$ describes the magnetic field vector per ampère current. $K_g$ is defined as the geometry factor to model the relation between the current $I_m$ and the magnetic field $\vec{H}_{opt}$ in the MOCS.

In [1], [2], and [3], concepts for optical current measurement systems based on multiple full rotations of the plane of polarisation (Faraday rotation $\Theta_F > 180°$) have been proposed. With a high optical rotation angle $\Theta_F$, a higher precision and a higher sensitivity can be achieved compared to concepts with less than $90°$ rotation angle. The rotation angle $\Theta_F$ is limited by trade-offs between the optical path length, the required measurement bandwidth, and the transmittance of the high-performance (high $\mathcal{V}$, low / inexistent magnetic saturation) magneto-optical material [1]. Therefore, the only parameter left to consider to increase the optical rotation angle is the magnetic field inside the optical path, i.e. the geometry factor $K_g$.
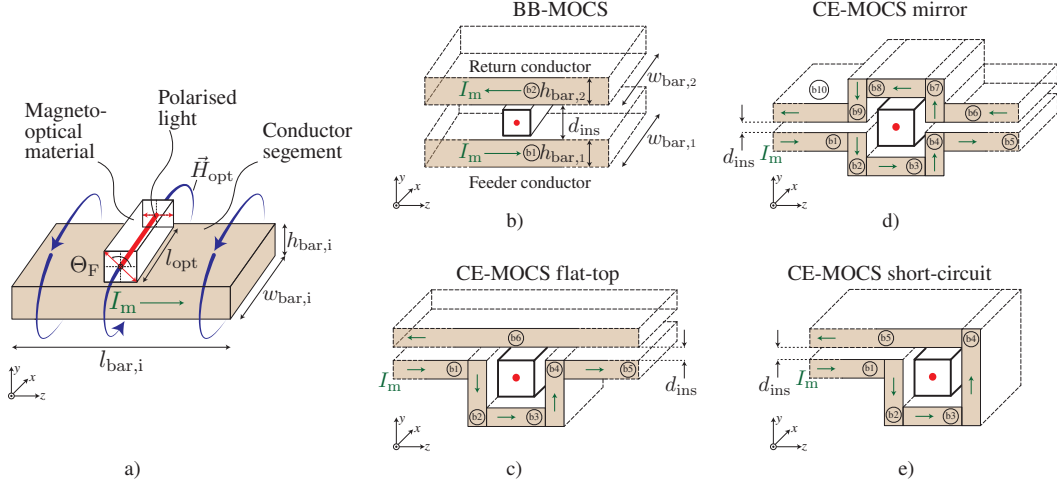
**Fig. 1:** a) The different busbar shapes are subdivided into rectangular conductor segments. A conductor segment $i$ is defined by its geometry parameters, i.e. the length $l_{bar,i}$, the width $w_{bar,i}$, and the height $h_{bar,i}$. The magnetic field of this conductor segment is then evaluated over the optical path of the MOCS. b) Busbar MOCS (BB-MOCS): Two parallel conductor with opposing current direction enclose the magneto-optical material. c) Cavity embedded MOCS (CE-MOCS) flat-top type: The magneto-optical material is enclosed tighter by the conductor to increase the magnetic field in the optical path. d) CE-MOCS mirror type: The return conductor is a mirror image of the feeder conductor. All conductor segments are arranged so that they contribute positively to geometry factor $K_g$. e) CE-MOCS short circuit type: The feeder conductor is directly connected to the return conductor. Almost the complete MO-material is surrounded by conductive material besides the slit required for the dielectric insulation.

In the past, different concepts to increase the magnetic field in the optical path of a bulk MOCS have been investigated. The most prominent example is a concentrator ring around the conductor [4, 5]. However, a ferromagnetic concentrator ring introduces saturation effects, hysteresis (non-linearities) and insulation problems between the conductor and the measurement system.

Another possibility to increase the magnetic field inside the optical path, and hence the optical Faraday rotation, is the optimisation of the conductor geometry. Therefore, the probe sensitivity of the optical current measurement system is maximised in this paper by increasing the overall optical Faraday rotation $\Theta_F$ through an optimisation of the conductor's geometry. This busbar modelling approach also provides a direct transfer function between the current $I_m$ and the measured Faraday rotation $\Theta_F$. For that purpose, the conductor geometry around the MOCS is defined to be a fixed part of the current measurement probe. In section 2, the optimisation procedure for the MOCS is shown. This optimisation procedure is based on an analytical model which is further explained in section 3. Section 4 shows the application of the derived model with respect to an example measurement system and discusses the optimisation results as well as the verification with a finite-element method (FEM) based model. Finally, the paper concludes in section 5.

## 2    Busbar Optimisation Procedure

The optimisation goal is an increased sensitivity of the optical current measurement probe. The sensitivity of the optical current measurement probe is the ratio of the optical rotation in degree per measured ampère current and it is a function of the geometry factor $K_g$:

$$S_p(K_g) = \frac{\Theta_F}{I_m} = \mathcal{V} \cdot K_g \tag{2}$$

In order to increase the sensitivity of the current measurement system, the geometry factor $K_g$ has to be maximised. First, different general busbar types, shown in Fig. 1, are discussed. Depending on the busbar shape, the magnetic field amplitude in the optical path can be increased, thereby increasing the geometry factor $K_g$ and the probe sensitivity $S_p$. The second step is subdividing the busbar into rectangular conductor elements, i.e. b1, b2, b3 and so forth. The contribution to $K_g$ of every conductor element is then optimised by varying the individual geometry parameters, i.e. the width $w_{bar,i}$ and the height $h_{bar,i}$. The geometry factor is calculated individually for every conductor segment ($K_{g,segment}$) and finally superposed to obtain the total busbar geometry factor $K_{g,busbar}$. This allows a more optimal distribution of the magnetic field
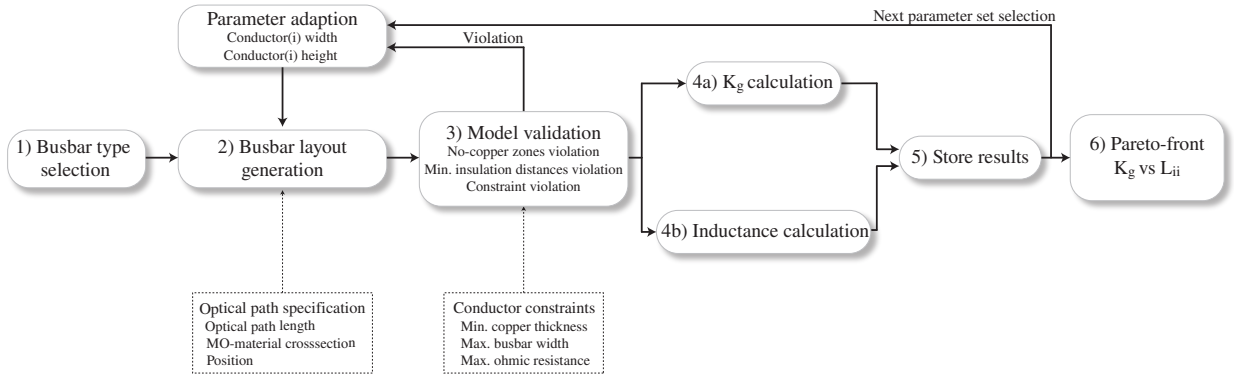
**Fig. 2:** A simplified flow-chart of the optimisation procedure is shown. The process validates the busbar geometry with respect to insulation distances, manufacturing constraints and ensures that no overlap between the conductor and the magneto-optical material occurs. The procedure results in a pareto-front comparing the busbar inductance and the busbar geometry factor $K_g$.

amplitude along the specified optical path in $x$-direction while minimising the insertion impedance of the overall busbar.

## Busbar Types

In order to increase the magnetic field in the optical path, the busbar shape is essential. The magnetic field in the optical path can be increased by moving the individual conductor segments closer to the MO-material and by making sure that all parts of the busbar generate a magnetic field in the same direction. In this section, the different busbar types shown in Fig. 1 are analysed. A comparison of the resulting $K_g$ is performed in section 4.

The busbar (BB-) MOCS shown in Fig. 1b) represents a standard configuration of two laminar conductors, a feeding and a return conductor. The two conductors enclose the MO-material on opposing sides and have opposing current directions. In contrast to the other busbar types in Fig. 1c) - e), two sides of the MO-material are not directly covered by a conductor which results in a lower magnetic field amplitude in the optical path. The minimal possible insulation distance $d_{ins}$ between the two conductors is directly determined by the MO-material height.

An improved busbar type is the cavity-embedded (CE-) MOCS that can be implemented in different ways. The MO-material is completely enclosed by conducting material in order to increase the current in close proximity to the optical path. Figure 1c) shows the CE-MOCS flat-top type in which the MO-material is completely enclosed by the feeding conductor. The magnetic fields generated by the conductor segments b1 and b5 have opposite directions in the optical path compared to the magnetic fields of the other conductors. The insulation distance $d_{ins}$ can be chosen to be as small as required by the insulation requirements. For high insulation requirements the distance between b6 and the feeder conductor needs to be increased, thereby decreasing the magnetic field in the optical path and increasing the insertion inductance.

Figure 1d) shows the CE-MOCS mirror type. Here, the return conductor is a mirror image of the feeder conductor with the $xz$-plane as mirror plane. In contrast to the CE-MOCS flat-top type, the horizontal bars b1, b5, b6 and b10 are located so that the generated magnetic field has the same direction as the rest of the arrangement. Hence, they contribute positively to the geometry factor $K_g$. The insulation distance $d_{ins}$ can again be chosen to be minimal according to the insulation requirements.

Finally, Fig. 1e) shows the CE-MOCS short circuit type which is especially interesting for designing and testing a prototype since no additional load is necessary. The conductor segments enclose almost all of the MO-material apart from the insulation region between the feeding and return conductor. In this arrangement, only b1 is not contributing positively to the geometry factor $K_g$.

In the next step, the $K_g$-related performance of these different busbar types is determined and optimised by a procedure focusing on the geometry parameters $w_{bar,i}$ and $h_{bar,i}$.

## Optimisation Procedure

The optimisation procedure shown in Fig. 2 is multi-objective and aims to maximise the geometry factor $K_g$ and to minimise the insertion impedance, which is dominated by the inductance $L_b$ of the busbar. The

variable parameters are the width ($w_{\mathrm{bar,i}}$) and height ($h_{\mathrm{bar,i}}$) of each conductor segment. The length of the busbar segment ($l_{\mathrm{bar,i}}$) is defined by the selected busbar type and the MO-material parameters, hence it is not a free parameter. Besides the optimisation goals, different constraints imposed by the manufacturing possibilities or electrical and optical requirements must be fulfilled.

Step 1 of the procedure is the choosing of a busbar type including the subdivision of the busbar into rectangular conductor segments. Here, as an example, the CE-MOCS flat-top type is chosen for the rest of this section and subdivided into six rectangular conductor segments as depicted in Fig. 3b).

In step 2, the individual busbar layout is generated. This means that the geometry parameters $w_{\mathrm{bar,i}}$ and $h_{\mathrm{bar,i}}$ of all rectangular conductor segments, in the considered example b1 – b6, are defined. Figure 3b) shows the different conductor segments widths and heights for a single layout of the CE-MOCS flat-top type. The busbar is further brought into context with the optical path specification, meaning that the distance between the center of each conductor segment and the center of the optical path is determined. This information serves as a reference for the calculation in the busbar model, which is explained in section 3. However, the optical path itself is not an optimisation subject in this procedure, although the determination of its parameters influences the outcome of the optimisation. A longer optical path length would enable the sensor head to capture more magnetic field, whereas a smaller cross-section would allow to place the busbar closer to the optical path, thereby increasing the geometry factor $K_{\mathrm{g}}$. Nevertheless, the optical path parameters have certain constraints, i.e the optical path length can not be extended indefinitely and the cross-section can not be made arbitrarily small. The optical transmission characteristics of the MO-material pose an upper limit to the optical path length since the transmission rate and the transmission velocity influence the measurement bandwidth and the measurement sensitivity. In [1], the optical measurement bandwidth and the optical transmission rate are modelled considering these material related characteristics. The MO-material cross-section is bound to a lower limit to ensure mechanical stability and to allow a minimal optical beam diameter.

In step 3, the considered busbar layout is validated with the constraints given in Tab. I and Tab. II. This includes checking the minimal and maximal copper thickness to ensure producibility. Thermal losses in the busbar pose a thermal limit which needs to be considered, although the considered operation is limited to very short pulse current applications. Additionally, it has to be made sure that the busbar geometry does overlap with the MO-material. If a violation occurs, the considered busbar layout and its parameter are discarded and the procedure restarts. After the validation check has been successfully completed, $K_{\mathrm{g}}$ and $L_{\mathrm{b}}$ for the considered busbar layout are determined.

In step 4a, the geometry factor $K_{\mathrm{g}}$ is calculated and solved with the analytical model given in section 3. The calculation is performed for every conductor segment of the busbar, i.e. b1 – b6 for the considered CE-MOCS flat-top type. The $K_{\mathrm{g,segment}}$ contributions of all six conductor segments are eventually superposed resulting in the total busbar $K_{\mathrm{g,busbar}}$. The busbar inductance is concurrently calculated in step 4b by applying the inductance model described in section 3. This includes the determination of all different busbar cross-sections, shown in Fig. 3b) for the CE-MOCS flat-top type example.

After storing the results in step 5 and repeating the procedure, the optimisation ends in step 6 and the $K_{\mathrm{g}}$ and $L_{\mathrm{b}}$ values return a pareto-optimal set of design points. In case of the CE-MOCS flat-top type, the pareto-optimal points are shown in Fig. 4a) and the geometry parameters for the best $K_{\mathrm{g}}$ point are given in Tab. III.

## 3 Analytical Model

The optimisation procedure presented in section 2 requires analytical models for the calculation of the geometry factor $K_{\mathrm{g}}$ and the busbar inductance $L_{\mathrm{b}}$. To calculate the geometry factor $K_{\mathrm{g}}$ analytically, a closed form for the magnetic field in the optical path is required. For this purpose, the busbar geometry is divided into rectangular conductor segments and the generated magnetic field in every point of the optical path is calculated with existing equations [6, 7]. These equations are applied to the integral form of the Faraday effect (1) which leads to a set of equations for the geometry factor contribution of each conductor segment. Finally, the contribution $K_{\mathrm{g,segment}}$ of every conductor element to the busbar geometry factor $K_{\mathrm{g,busbar}}$ is superposed.

To calculate the busbar inductance $L_{\mathrm{b}}$, a model based on the analytical calculation of the inductance per unit length from [8] is used. The inductance per unit length is then calculated for each cross-section of
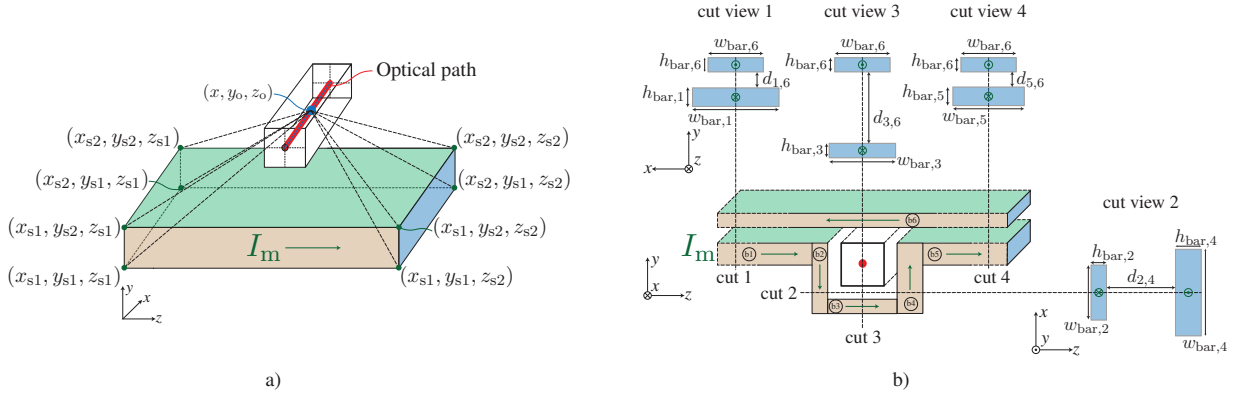
**Fig. 3:** a) The magnetic field of a rectangular conductor segment with a constant current density can be analytically calculated in every point of the optical path (red line). The geometry factor $K_g$ is a function of the distance between the conductor segment and the optical path. The distance is determined by the position of the optical path $(x, y_0, z_0)$ and all eight vertices of the conductor segment. b) The CE-MOCS flat-top type has four different cross-sections that need to be taken into account for the inductance calculation. Cut view 1 to cut view 4 show the individual busbar cross-sections so that their respective conductor segment width $w_{bar,i}$ and height $h_{bar,i}$ can be distinguished. The distance $d_{i,j}$ shows the distance between two conductor segments and is required to determine the inductance $L_b$.

the busbar. A cross-section is defined to cut the busbar so that the currents are through-plane as shown in Fig. 3b). This cross-section is then parameterised by the conductor segments based on $(w_{bar,i})$ and height $(h_{bar,i})$, as well as the distance $d_{i,j}$ between the conductor segments in this cross-sectional cut.

In the following section, the equations for $K_g$ are derived and explained with the example of the CE-MOCS flat-top type.

## Geometry Factor $K_g$ of a Busbar

The analytical equations for the magnetic field of a rectangular conductor segment with a finite volume are based on the Green functions as the solution of the Poisson equation [6, 7, 9]. Here, the equation from [7] is rewritten in (4) based on a vectorised, analytical implementation. The current $I_m$ is assumed to be a constant (DC-case) and to have only a positive $z$-component, as shown in Fig. 3a). For those conductor segments that have a different current direction than the positive $z$-direction a coordinate transformation is necessary after the calculation of the magnetic field. In the CE-MOCS flat-top type these are the conductor segments b2, b4, and b6. Since the current only has a $z$-component, based on Ampères law, the magnetic vector potential has also only a $z$-component and the magnetic field is zero in $z$-direction.

$$A_x = A_y = 0 \qquad\qquad B_z = 0 \qquad\qquad (3)$$

The remaining two components of the magnetic field in every point of the optical path are then given by (4):

$$\vec{B}_{opt}(x, y_0, z_0) = I_m \cdot \vec{b}_g(x, y_0, z_0)$$

$$= I_m \begin{bmatrix} \frac{\mu_0}{4\pi A_{cr}} \sum\limits_{i,j,k=1}^{2} (-1)^{i+j+k} \left( -\gamma_k \operatorname{artanh}\left(\frac{\alpha_i}{r_{i,j,k}}\right) - \alpha_i \operatorname{artanh}\left(\frac{\gamma_k}{r_{i,j,k}}\right) + \beta_j \arctan\left(\frac{\alpha_i \gamma_k}{r_{i,j,k} \beta_j}\right) \right) \\ \frac{\mu_0}{4\pi A_{cr}} \sum\limits_{i,j,k=1}^{2} (-1)^{i+j+k} \left( \gamma_k \operatorname{artanh}\left(\frac{\beta_j}{r_{i,j,k}}\right) + \beta_j \operatorname{artanh}\left(\frac{\gamma_k}{r_{i,j,k}}\right) - \alpha_i \arctan\left(\frac{\beta_j \gamma_k}{r_{i,j,k} \alpha_i}\right) \right) \\ 0 \end{bmatrix} \qquad (4)$$

with

$$\alpha_i = x - x_{s,i} \qquad\qquad \beta_j = y_0 - y_{s,j} \qquad\qquad \gamma_k = z_0 - z_{s,k}$$

$$r_{i,j,k} = \sqrt{\alpha_i^2 + \beta_j^2 + \gamma_k^2} \qquad\qquad A_{cr} = (x_{s,2} - x_{s,1}) \cdot (y_{s,2} - y_{s,1}) \qquad (5)$$

In (4) and (5), the following expressions are used:
- $I_m = I_z$ is the constant current in $z$-direction.
- $x_{s,i}, y_{s,j}, z_{s,k}$ with $i, j, k = [1, 2]$ are the integration boundaries of the source (conductor) as shown in Fig. 3a).
- $x$ is the free and $y_0, z_0$ are the fixed spatial parameters of the optical path.
- $A_{cr}$ is the rectangular cross-section surface as defined in (5).

With (1), (4), and (5), a closed form for the geometry factor of a single segment $K_{\mathrm{g,segment}}$ can be determined by integrating $\vec{b}_{\mathrm{g}}$ over the optical path length. According to (1) only the magnetic field in the direction of the optical path is considered to influence the optical rotation angle $\Theta_{\mathrm{F}}$. Since the optical path only extends in $x$-direction, only the integration over the $x$-component of the magnetic field has to be considered. Hence, the geometry factor of a single segment $n$, as for example segment b3 in the CE-MOCS flat-top type shown in Fig. 3a), is calculated with:

$$\Theta_{\mathrm{F}} \propto K_{\mathrm{g,segment},n} = \int_{\mathcal{P}} \vec{b}_{\mathrm{g}}(x,y_{\mathrm{o}},z_{\mathrm{o}}) \cdot \mathrm{d}\vec{l}_{\mathrm{opt}} = \int_{\mathcal{P}} b_{\mathrm{g,x}}(x,y_{\mathrm{o}},z_{\mathrm{o}}) \, \mathrm{d}x$$

$$= \sum_{i,j,k=1}^{2} (-1)^{i+j+k} \left[ \int_{\mathcal{P}} f_1(x,y_{\mathrm{o}},z_{\mathrm{o}}) \, \mathrm{d}x + \int_{\mathcal{P}} f_2(x,y_{\mathrm{o}},z_{\mathrm{o}}) \, \mathrm{d}x + \int_{\mathcal{P}} f_3(x,y_{\mathrm{o}},z_{\mathrm{o}}) \, \mathrm{d}x \right] \tag{6}$$

$$= \sum_{i,j,k=1}^{2} (-1)^{i+j+k} \left[ F_1(x,y_{\mathrm{o}},z_{\mathrm{o}}) + F_2(x,y_{\mathrm{o}},z_{\mathrm{o}}) + F_3(x,y_{\mathrm{o}},z_{\mathrm{o}}) \right]$$

where $f_1$, $f_2$, and $f_3$ represent terms in the first row of the vector in (4) and $F_1$, $F_2$, and $F_3$ are the analytical solutions to the integration of these terms. Note that the order of the sum and the integral have been changed based on the theorem of Fubini/Tonelli. The analytical solutions for the integrals in (6) with the expressions from (4) are:

$$F_1(x,y_{\mathrm{o}},z_{\mathrm{o}}) = \int_{\mathcal{P}} f_1(x,y_{\mathrm{o}},z_{\mathrm{o}}) \, \mathrm{d}x = -\gamma_k \cdot \left[ \mathrm{artanh}\left( \frac{\alpha_i}{r_{i,j,k}} \right) \cdot \alpha_i - r_{i,j,k} \right]_{l_{\mathrm{opt}}}$$

$$F_2(x,y_{\mathrm{o}},z_{\mathrm{o}}) = \int_{\mathcal{P}} f_2(x,y_{\mathrm{o}},z_{\mathrm{o}}) \, \mathrm{d}x = \frac{1}{2} \left[ \mathrm{artanh}\left( \frac{r_{i,j,k}}{\gamma_k} \right) \cdot \gamma_k^2 - \gamma_k \cdot r_{i,j,k} - \mathrm{artanh}\left( \frac{\gamma_k}{r_{i,j,k}} \right) \cdot r_{i,j,k}^2 \right]_{l_{\mathrm{opt}}} \tag{7}$$

$$F_3(x,y_{\mathrm{o}},z_{\mathrm{o}}) = \int_{\mathcal{P}} f_3(x,y_{\mathrm{o}},z_{\mathrm{o}}) \, \mathrm{d}x = \beta_j \cdot \left[ \beta_j \cdot \mathrm{artanh}\left( \frac{\beta_j r_{i,j,k}}{\gamma_k \beta_j} \right) + \alpha_i \cdot \arctan\left( \frac{\gamma_k \alpha_i}{\beta_j r_{i,j,k}} \right) \right]_{l_{\mathrm{opt}}}$$

The solutions in (6) and (7) represent the equation for the geometry factor of a single rectangular conductor segment, as for example the conductor segment b3 of the CE-MOCS flat-top type shown in Fig. 3a). The geometry factor of a segment is a single scalar value. Since no core material is present and the MO-material is paramagnetic [1] linearity is given and the geometry factor $K_{\mathrm{g,busbar}}$ of the complete busbar can then be calculated by the superposition of the solution of every single conductor segment $n$ in the complete busbar, i.e.:

$$K_{\mathrm{g,busbar}} = \sum_{n \in \text{Busbar}} K_{\mathrm{g,segment},n} \tag{8}$$

This model of the geometry factor directly links the optical rotation angle and the geometric parameters of the busbar. Furthermore, the model consists of only closed form analytical equations, hence, determining the $K_{\mathrm{g,busbar}}$-value does not require computationally intensive calculations.

## Inductance Calculation for Busbar Cross-sections

In order to limit the influence of the current measurement probe on the system under test, the total inductance of the busbar needs to be minimised, as indicated by step 4b of the optimisation procedure. Here, the model from [8] is applied to calculate the inductance per unit length of a busbar cross-section. The model assumes rectangular conductor cross-sections with a constant through-plane current density as shown in Fig. 3b) and considers flux fringing around the conductor. A detailed description of the model and the implementation can be found in [10].

The model parameter are again the busbar width $w_{\mathrm{bar,i}}$ and height $h_{\mathrm{bar,i}}$ that define the respective busbar cross-section. The inductance also depends on the distance $d_{\mathrm{i,j}}$ between the two conductor cross-sections, as shown in Fig. 3b).

Figure 3b) shows all cross-sections of the CE-MOCS flat-top busbar type configuration. The inductance per unit length $L_{\mathrm{b}}'$ can be calculated with the model in [8] for every cross-section in the busbar. Hence, it is necessary to find the set of cross-sections, i.e. cut 1 – cut 4, and to calculate the inductance per unit length $L_{\mathrm{b}}'$ for all these cross-sections. As an example, cut 1 is defined by the width and height of conductor segment 1 and 6. This cross-section is the same for the complete length $l_{\mathrm{cs,16}}$ of conductor segment 1. The model returns the inductance per unit length that is then multiplied with the length $l_{\mathrm{cs,16}}$ in which the cross-section is the same. Eventually, the final inductance $L_{\mathrm{b}}$ is the sum of the contribution from all busbar
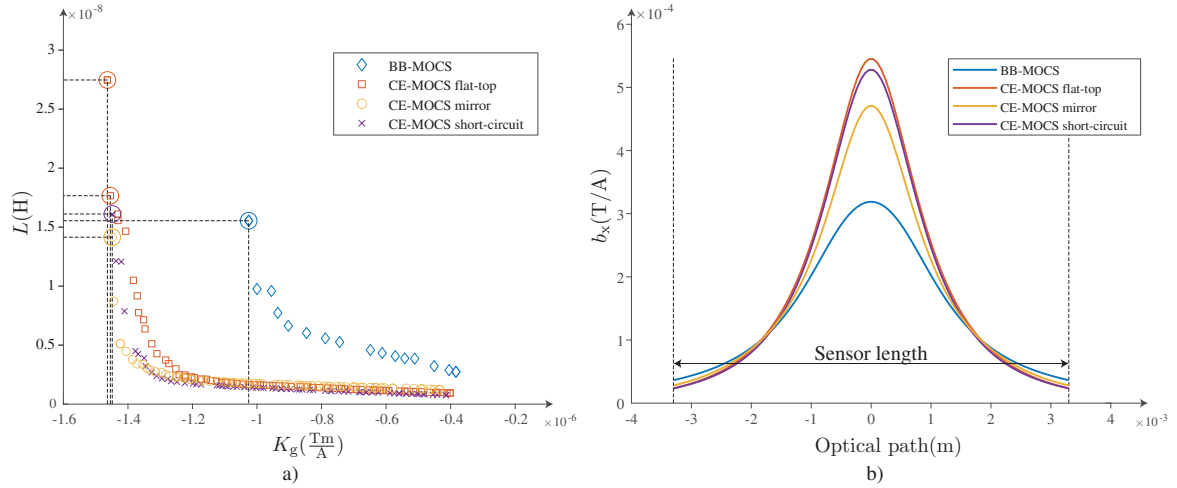
**Fig. 4:** a) Pareto-front of the busbar design showing the trade-off between the geometry factor $K_g$ and the inductance $L_b$. Note that only the absolute value of $K_g$ is of interest since the sign only defines the rotation direction of the plane of polarisation. b) The chosen design points for each busbar type show different magnetic field distribution over the optical path. In order to achieve an optimal $K_g$, a high magnetic field is required inside and a low magnetic field outside the MO-material.

cross-sections given by cut view 1 – cut view 4 in Fig. 3b).

# 4    Model Application and Optimisation Results

In this section, the busbar types shown in Fig. 1 are optimised with the optimisation procedure given in section 2. The system requirements and the design constraints are listed in Tab. I and Tab. II. Furthermore, the results for the busbar types are compared and the most promising result is verified with FEM.

## Optimisation Results

The optimisation leads to a set of pareto-optimal points as depicted in the pareto-front in Fig. 4. The considered geometry parameter ranges and the results for $K_g$ and $L_b$ of the presented design points are given in Tab. III.

The BB-MOCS in Fig. 1b) serves as the benchmark geometry. This geometry type results in the lowest $K_g$ while having a relatively high inductance value. The free space around the MO-material on the left and on the right side limits the achievable $K_g$. The inductance of this type is large since the minimal distance $d_{ins}$, defined by the MO-material height, spans a large surface amongst the two conductors. The pareto-front in Fig. 4a) shows that a geometry factor of $K_g = 1.02 \cdot 10^{-6}$Tm/A can be achieved with the constraints given in Tab. II. This point corresponds to an inductance of $L_b \approx 15.5$ nH.

To increase the Faraday rotation per ampère current, the CE-MOCS encloses the magneto-optical material to a higher extend. The CE-MOCS flat-top type achieves a maximal $K_g = 1.47 \cdot 10^{-6}$Tm/A. The inductance $L_b \approx 27.4$ nH exceeds the maximal allowable inductance given by the specifications. A design point with less $K_g$ but an inductance inside the design specifications is given with $K_g = 1.46 \cdot 10^{-6}$Tm/A and

**Table I:** System requirements

|  | Value | Units |
|---|---|---|
| Current range | $0 < I_m \leq 1000$ | A |
| Current form | Pulsed | |
| Supply voltage | $V_{DC} \leq 800$ | V |
| Maximal inductance | $L_b \leq 24$ | nH |
| Minimal pulse rise time | $0.03 \leq t_r \leq 1$ | µs |
| Measurement bandwidth | $DC < w_m \leq 12$ | MHz |
| Full bandwidth uncertainty | $< 0.1$ | % |
| Reproducibility error | 25 | ppm |

**Table II:** Constraints

|  | Value |
|---|---|
| *Magneto-optical material constraints / parameter* | |
| Composition $Cd_xMn_yTe$ | $x = 0.57, y = 0.43$ |
| Verdet constant $\mathcal{V}$ @ 660 nm | $150°/(Tmm)$ |
| Length $l_{opt}$ | 6.6 mm |
| Width $w_{opt}$ | 2.3 mm |
| Height $h_{opt}$ | 2.3 mm |
| *Conductor constraints* | |
| Minimal copper thickness | 0.2 mm |
| Maximal copper thickness | 20 mm |
| Minimal insulation distance | 0.27 mm |

**Table III:** Optimisation results: The segment width and height given in this table correspond to the respective busbar segment shown in Fig. 1. For example, the first value in the segment width list corresponds to b1 in the figure and so forth.

| Busbar type | $K_g$ | $L_b$ | # Segment | Segment width | Segment height |
|---|---|---|---|---|---|
| BB-MOCS | $1.02 \cdot 10^{-6}$ Tm/A | 15.5 nH | 2 | $[1.4, 1.3]$ mm | $[1.1, 0.2]$ mm |
| CE-MOCS flat-top | $1.46 \cdot 10^{-6}$ Tm/A | 17.5 nH | 6 | $[19.9, 0.7, 1.1, 1.5, ...$ $19.5, 3.5]$ mm | $[0.2, 1.1, 1.1, 0.2, ...$ $0.2, 0.2]$ mm |
| CE-MOCS mirror | $1.45 \cdot 10^{-6}$ Tm/A | 14.1 nH | 10 | $[2.5, 4.8, 0.4, 0.9, 0.5, ...$ $0.8, 0.7, 0.6, 0.7, 0.7]$ mm | $[0.1, 1.0, 1.1, 1.4, 0.2, ...$ $1.5, 0.3, 1.2, 1.1, 0.5]$ mm |
| CE-MOCS short-circuit | $1.44 \cdot 10^{-6}$ Tm/A | 16.1 nH | 5 | $[19.9, 0.7, 0.4, 0.3, 0.4]$ mm | $[0.2, 1.1, 1.2, 0.2, 0.2]$ mm |

$L_b \approx 17.5$ nH, which provides a better trade-off between the two optimisation goals. The main advantage of this busbar type is that the conductors on the side of the MO-material (b2, b4) fully cover the side and contribute to the magnetic field in negative *x*-direction. The conductors b1 and b5 reduce the magnetic field since the direction of their magnetic field in the optical path is opposite to the contribution of b2, b3 and b4. Hence, the conductor segments b1 and b5 become very wide during the optimisation in order to reduce their negative influence on the $K_g$ value and to reduce the busbar inductance.

The CE-MOCS mirror type shown in Fig. 4d) results in $K_g = 1.45 \cdot 10^{-6}$ Tm/A. This design point has an inductance of $L_b \approx 14.1$ nH. Here, the conductor segments b1, b5, b6, and b10 all increase the $K_g$-value since their relative position to the optical path in combination with their individual current direction leads to a magnetic field pointing in the same direction as the remaining conductor segments. In comparison to the CE-MOCS flat-top type, the CE-MOCS mirror type results in a comparable $K_g$ but in a lower inductance. The reason is that the height of the largest cross-section between b3 and b8 is directly limited by the sensor height. On the other hand, the CE-MOCS flat-top type includes the additional insulation distance into this cross-section between the segments b3 and b6 which leads to a higher inductance value.

Finally, the CE-MOCS short circuit type results in $K_g = 1.44 \cdot 10^{-6}$ Tm/A. This design point results in an inductance value of $L_b = 16.1$ nH. The design is closely related to the CE-MOCS flat-top type, only the conductor segments connecting to a load are omitted. In terms of $K_g$, this type provides the same results as the CE-MOCS flat-top type and is therefore of particular interest for a test set-up with a short circuit as load.

Note that in order to increase $K_g$ the yet straight conductor segments could be subdivided into multiple conductor segments to allow the optimisation to find a better trade-off. For example, the conductor segment b6 of the CE-MOCS flat-top could be subdivided into three conductor segments b6a, b6b, and b6c, where b6b is located directly over the MO-material. This would allow the optimisation to return a very small cross-section for b6b while b6a and b6c can be kept at the maximal allowed width to reduce the overall inductance value. Since this busbar is already divided into small segments, it has to be considered, that the overall impact is not large and the manufacturing process becomes more complicated since the shape would have to be adapted multiple times.

**Result Discussion**

With $K_g$, the probe sensitivity $S_p$ and the total rotation angle $\Theta_F$ can be determined with (1) and (2) which contains the scaling factor $\mathcal{V}$, i.e. the Verdet constant. The chosen MO-material, CdMnTe, has a Verdet constant of $\mathcal{V} = 150 \cdot 10^{3\circ}$/Tm. A change of the geometry factor of $\Delta K_g = 10^{-7}$ Tm/A can be translated to a change of the optical rotation per ampére current $S = 0.015\,°$/A.

The optimisation results for the BB-MOCS and the CE-MOCS flat-top busbar types show a $K_g$ improvement of 43.1 % or $\Delta K_g = 4.4 \cdot 10^{-7}$ Tm/A with the chosen constraints. Hence, the sensitivity is increased by $\Delta S = 0.066\,°$/A. In case of the specified prototype given in table I, a Faraday rotation angle improvement of at least $\Delta\Theta_F = 66°$ can be achieved. The optical rotation improvement directly relates to a resolution improvement as described in [2].

The results of the inductance calculation show that the inductance values remain roughly the same for the different busbar types. In fact, the best CE-MOCS flat-top type results in a lower inductance due to the improved layout of the cross-sections and the minimised distance $d_{i,j}$ between the conductors.

The different CE-MOCS busbar types do not differ substantially in terms of $K_g$. However, the CE-MOCS flat-top type is advantageous in terms of its applicability in high power busbar systems. Considering hig-
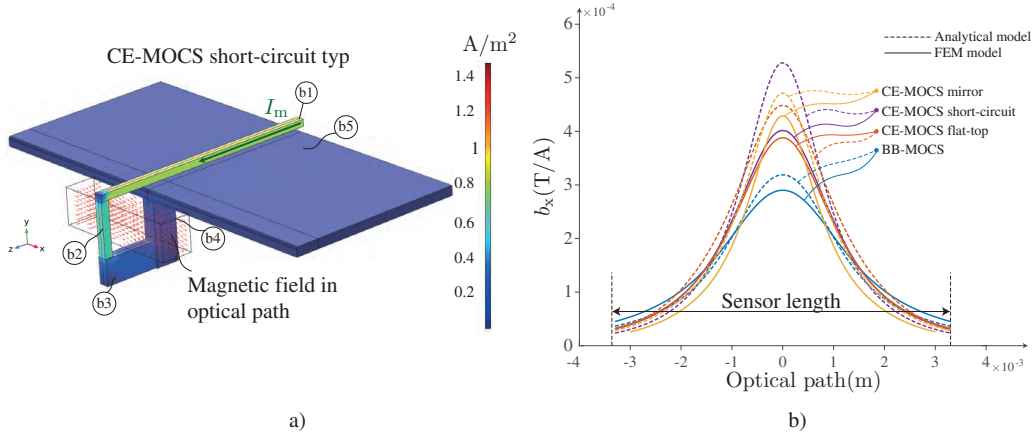
**Fig. 5:** a) The FEM model for the CE-MOCS short circuit shows that the current density is not constant in the corner regions. This leads to a different magnetic field distribution in the optical path compared to the analytical model. b) The magnetic field distribution of the analytical model matches with the FEM results. The difference between the two results is mainly explained by the non-constant current density in the busbar cross-sections which is considered in the FEM simulation but not in the analytical model.

her input voltages between the feeding and the return conductor for very fast pulse current applications, the CE-MOCS mirror type shows considerable drawbacks in terms of insulation. While an insulation can be used between the complete length of the CE-MOCS flat-top types feeding and return conductor, the construction of such a layer becomes much more difficult for the CE-MOCS mirror type. Further, such an insulation layer cancels the CE-MOCS mirror types advantage of having the conductors b1, b5, b6, and b10 close to the MO-material and contributing positively to the magnetic field.

## FEM Verification

In the following, the best evaluated design points of the proposed busbar types are verified with a stationary FEM simulation which considers a steady-state DC current. The results are shown in Tab. IV. Since the BB-MOCS essentially consists of two straight bars and no busbar bends, the analytical model is expected to accord well with the FEM simulation. However, a peak magnetic field difference between the analytical and the FEM model $\Delta B_{\mathrm{x,peak}} = 9.4\,\%$ is shown in Fig. 5b) and the $K_{\mathrm{g}}$ values differ by $\Delta K_{\mathrm{g}} = 14.73\,\%$. The main reason for this difference is that the FEM model includes a non-homogenous current density and the coupling influences of the different busbar segments on each other. On the other hand, the analytical model considers a constant current density in the busbar and neglects the influence of the different segments on the current distribution.

The same is true for the CE-MOCS busbar types. The $K_{\mathrm{g}}$ error from the analytical model is in the range of 20 % depending on the chosen busbar type. The non constant current-densities which are considered in the FEM simulation change the magnetic field distribution. For those busbar types the corner regions have a significant influence on the current density distribution in the respective cross-section.

Eventually, the analytical model enables a good comparison between the different busbar types, which allows to identify the best busbar type. However, the result accuracy of the analytical model suffers directly from the simplified current density distribution.

**Table IV:** Comparison of analytical and FEM $K_{\mathrm{g}}$ results

| Busbar type | $K_{\mathrm{g}}$ Analytical | $K_{\mathrm{g}}$ FEM | $\Delta K_{\mathrm{g}}$ |
|---|---|---|---|
| BB-MOCS | $1.02 \cdot 10^{-6}\mathrm{Tm/A}$ | $0.88 \cdot 10^{-6}\mathrm{Tm/A}$ | 14.73 % |
| CE-MOCS flattop | $1.46 \cdot 10^{-6}\mathrm{Tm/A}$ | $1.2 \cdot 10^{-6}\mathrm{Tm/A}$ | 19.54 % |
| CE-MOCS mirror | $1.45 \cdot 10^{-6}\mathrm{Tm/A}$ | $1.15 \cdot 10^{-6}\mathrm{Tm/A}$ | 23.07 % |
| CE-MOCS short circuit | $1.44 \cdot 10^{-6}\mathrm{Tm/A}$ | $1.18 \cdot 10^{-6}\mathrm{Tm/A}$ | 19.77 % |

# 5 Conclusion

The sensitivity of a magneto-optical current sensor is increased by a locally maximised magnetic field along the optical path. The geometry factor $K_g$ is introduced to relate the measured Faraday rotation angle and the sensitivity directly to the measured current in the conducting geometry.

To evaluate and subsequently optimise the geometry of the busbar, analytical equations for the geometry factor $K_g$ are derived in this paper. These equations integrate the complete magnetic field in the optical path of the magneto-optical material. Additionally, analytical equations for the calculation of the busbar inductance are applied to calculate the total insertion impedance of a busbar.

In total, four different busbar types are evaluated, the BB-MOCS, the CE-MOCS flat-top type, the CE-MOCS mirror type, and the CE-MOCS short-circuit type. The factor $K_g$ improves by more than $43\%$ when a CE-MOCS instead of a BB-MOCS busbar type is chosen. However, the difference between the three CE-MOCS busbar types is not significant.

Eventually the analytical model is verified with a FEM simulation. The FEM simulation results show a deviation of $< 20\%$ which is explained by the assumption of a constant current distribution in the analytical model. However, the analytical model enables to compare the different busbar types and to identify the best busbar parameters.

## Acknowledgement

## References

[1] S. Rietmann and J. Biela, "Sensor Design for a Current Measurement System with High Bandwidth and High Accuracy Based on the Faraday Effect," in *21nd Eur. Conf. on Power Electron. and Appl. (EPE ECCE Europe)*, 2019.

[2] ——, "Error Induced by the Optical Path of a High Accuracy and High Bandwidth Optical Current Measurement System," in *22nd Eur. Conf. on Power Electron. and Appl. (EPE ECCE Europe)*, 2020.

[3] D. Gerber and J. Biela, "High-dynamic and High-precise Optical Current Measurement System Based on the Faraday Effect," *IEEE Plasma Sci.*, vol. 43, no. 10, pp. 3550–3554, 2015.

[4] G. Li, M. G. Kong, G. R. Jones, and J. W. Spencer, "Sensitivity Improvement of an Optical Current Sensor with Enhanced Faraday Rotation," *J. Lightw. Technol.*, vol. 15, no. 12, pp. 2246–2252, 1997.

[5] L. Shen-Wang, Z. Guo-Qing, Y. Wen-Bin, G. Zhi-Zhong, S. Yan, Z. Yi-Nan, C. Song, and L. Hong-Kai, "Optimization Design of Optical Current Sensor with Magnetic Concentrator Ring for Gas Insulated Switchgear," in *2nd Int. Conf. on Instrum., Meaus., Comp., Comm. and Cont.*, 2012.

[6] L. Urankar, "Vector Potential and Magnetic Field of Current-carrying Finite Arc Segment in Analytical Form, Part III: Exact Computation for Rectangular Cross Section," *IEEE Trans. Magn.*, vol. 18, no. 6, pp. 1860–1867, 1982.

[7] E. Rochepault, G. Aubert, P. Vedrine, and F. Bouillault, "3D Magnetic Optimization of Dipole Ends with Rectangular Cross-sections," *EPJ Appl. Phys.*, vol. 64, no. 2, p. 24507, 2013.

[8] X. Margueron, A. Besri, P.-O. Jeannin, J.-P. Keradec, and G. Parent, "Complete Analytical Calculation of Static Leakage Parameters: A step Toward HF Transformer Optimization," *IEEE Trans. Ind. Appl.*, vol. 46, no. 3, pp. 1055–1063, 2010.

[9] S. J. Sackett, "Calculation of Electromagnetic Fields and Forces in Coil Systems of Arbitrary Geometry," Lawrence Livermore Lab., Univ. of California, Report, 1975.

[10] R. Schlesinger and J. Biela, "Comparison of Analytical Models of Transformer Leakage Inductance: Accuracy vs. Computational Effort," *IEEE Trans. Power Electron.*, 2020.